IOP Publishing Smart Materials and Structures
Smart Mater. Struct. **28** (2019) 065010 (11pp) https://doi.org/10.1088/1361-665X/ab14b1

Least-squares reverse time migration (LSRTM) for damage imaging using Lamb waves

Jiaze He[1,2], Daniel C Rocha[3], Patrick E Leser[4], Paul Sava[3] and William P Leser[4]

[1] National Institute of Aerospace, Hampton, VA 23666, United States of America
[2] North Carolina State University, Raleigh, NC, 27695, United States of America
[3] Center for Wave Phenomena, Colorado School of Mines, Golden, CO, 80401, United States of America
[4] NASA Langley Research Center, Hampton, VA, 23681, United States of America

E-mail: jiazeh@princeton.edu

Received 22 November 2018, revised 13 March 2019
Accepted for publication 29 March 2019
Published 1 May 2019

Abstract

Large-area monitoring and accurate damage quantification are two primary goals of ultrasonic, guided wave-based structural health monitoring (SHM). Reverse-time migration (RTM) is an effective damage imaging technique for both metallic and composite plates. In geophysics, incorporating least-squares inversion into migration can generate images with higher resolution and suppressed artifacts in comparison with conventional RTM. Development of a least-squares reverse time migration (LSRTM) technique is promising for SHM since it could expand the imaging area for a given sensor array while maintaining a relatively high resolution. An LSRTM technique is introduced in this research for damage imaging in an isotropic plate using A_0 mode Lamb waves. A finite difference algorithm based on the Mindlin plate theory was used to simulate the flexural wave propagation. To form the theoretical foundations for guided wave-based LSRTM, a forward modeling operator and its adjoint are defined. The damage images from both numerical simulations and experiments show that LSRTM can enhance imaging resolution and reduce artifacts.

Keywords: least-squares reverse-time migration (LSRTM), damage imaging, inverse problem, guided waves, ultrasonic waves

(Some figures may appear in colour only in the online journal)

1. Introduction

As the maintenance cost of engineering structures increases [1, 2], so does the need for rapid nondestructive evaluation (NDE) and quantitative structural health monitoring (SHM) [3]. These technologies provide continuous health state awareness and enable more informed maintenance practices, such as condition-based maintenance [4]. Ultrasonic guided waves have received significant attention in the past two decades, particularly in the field of SHM [5] as a result of their ability to propagate over long distances and areas, and provide through-thickness information [6]. These characteristics, combined with a data acquisition system and an imaging algorithm, have the potential to yield rapid NDE and quantitative SHM.

A key component of a data acquisition system is its transducers. Different transducer types are suitable for various ultrasonic guided wave applications. Excitation or reception components can be piezoelectric wafers [7, 8], shear-horizontal transducers [9, 10], polyvinylidene difluoride (PVDF) transducers [11], air-coupled transducers [12, 13], pulsed-laser [14] and laser Doppler vibrometer (LDV) [15]. The patterns for transducer distribution vary from sparse array [16] to densely distributed arrays [17, 18], and full-aperture array [19, 20].

The other critical aspect of a successful guided wave-based SHM or NDE system is an effective imaging algorithm.

 © 2019 IOP Publishing Ltd Printed in the UK

A variety of algorithms have been studied to provide damage detection and quantitative imaging using guided waves. Time-of-flight-based triangulation and its variations [14, 21] are typically used for damage localization. Delay-and-sum [22] can approximate damage sizes [23], especially with additional features in imaging algorithm design such as minimum-variance estimation [24] and damage distribution probability [25].

Improved accuracy can be achieved with the consideration of diffraction effects using diffraction tomography [26, 27]. A hybrid algorithm for robust breast ultrasound tomography [28], based on theoretical Green's functions, utilize the diffraction tomography as an initial model of a scattering object. This scattering model is then iteratively updated to further improve the resolution. As studied by Rose *et al* in [29], time-reversal (TR) can be related to diffraction tomography. Originating in general ultrasonics [30], TR is based on the decomposition of the TR operator to extract singular values corresponding to different scatterers. With an imaging condition called MUltiple SIgnal Classification, TR can achieve resolution finer than half of the input wavelength (super-resolution) [31, 32]. However, artifacts have been observed for this method when encountering finite-sized (compared with wavelength) targets including damage sites, since the theory was derived for point-like scatterers [33].

For damage comparable to or larger than the wavelength, reverse-time migration (RTM) has been proven to be an effective guided wave-based damage imaging technique [29, 34]. RTM originated in the field of geophysics [35, 36]. It is based on two-way wave equations, which can more accurately characterize complex scattering paths as well as steeply dipping faults by reducing kinematic errors [37]. For the same reasons, when used as an ultrasonic NDE and SHM technique, RTM is suitable for imaging data acquired in structures with complex geometries [38, 39] and to image damage with complex signatures such as multiple modes scattering effects [40]. Similar to diffraction tomography, RTM can also generate images with physical meaning (e.g. damage reflectivity, obtained from a normalized zero-lag cross-correlation (ZLCC) imaging condition [15, 41]. Some imaging conditions that can potentially be used in conjunction with guided wave RTM are based on displacement wavefield [42], scalar wavefield [43], or energy norms [44–46].

While RTM has demonstrated early success in the field of SHM, RTM images often contain various undesirable artifacts when bandwidth and sensor coverage are limited. This problem is not unique to RTM technique but does hinder the technique for real-world applications with limited sensor coverages. Least-squares migration (LSM) is an imaging algorithm that reduces these migration artifacts and also improves the resolution of migrated images. LSM is a linearized waveform inversion that has been used to find the image that best predicts, in a least-squares sense, the recorded seismic data [47, 48]. When LSM uses an RTM engine, it is referred to as least-squares reverse-time migration (LSRTM) [49–51].

The main purpose of this paper is to explore LSRTM as an SHM technique for imaging damage in plate-like structures. The work focused on Lamb wave, a particular type of ultrasonic guided wave, common to the field of SHM. The goal of the work is to demonstrate higher resolution and higher degrees of artifact suppression compared to conventional RTM imaging. The remainder of this paper is organized as follows: first, the theory of LSRTM is derived in the context of ultrasonic guided waves. Then an efficient optimization algorithm, the conjugate gradient (CG) method, is introduced. The method was used to implement the LSRTM technique. Finally, numerical and experimental results from LSRTM are compared with the images obtained from conventional RTM.

2. LSRTM theory

The process of traditional RTM contains three parts: the forward wavefield simulation, the back-propagation of the time-reversed received signals, and the application of imaging conditions [17]. As mentioned earlier, a normalized ZLCC imaging condition [15] in RTM can generate the reflectivity or the reflective coefficients of the damaged region. This physical meaning of the image is particularly useful because it can be converted to plate thickness loss or stiffness change through dispersion relations such that damage severity can be quantified as well [52].

In this research, with the selected damage model parameter as its reflectivity $\mathbf{m}$, which is defined as the amplitude ratio between the reflected waves and the incident waves, LSRTM theory is developed in the context of guided wave-based damage imaging.

Forward modeling is the process of generating the damage-scattered waves via numerical simulation using a model of the damaged component or structure being monitored. This process generates the signals to be compared with experimental measurements. The next subsection introduces the procedures to convert the discrepancy between the measured data and the simulated data to quantitative model updates for each iteration.

Mathematically, the forward modeling process can be represented by a formal modeling operator $\mathbf{F}$ as:

$$\mathbf{d}_{obs} = \mathbf{F}\mathbf{m}_{true}, \tag{1}$$

where $\mathbf{d}_{obs}$ is the received damage-scattered data at the sensor array, and in this research, only a single source is used such that there is only one forward wavefield generation during this process. Then the migration imaging is the adjoint of the forward modeling [36], which can be expressed as

$$\mathbf{m}_{mig} = \mathbf{F}^T\mathbf{d}_{obs}, \tag{2}$$

where $\mathbf{F}^T$ is the adjoint operator that transforms received data $\mathbf{d}_{obs}$ into the image $\mathbf{m}_{mig}$. From equations (1) and (2), the relationship between the migration image and the true reflectivity image [53] is

$$\mathbf{m}_{mig} = \mathbf{F}^T\mathbf{F}\mathbf{m}_{true}. \tag{3}$$

Theoretically, the true reflectivity image $\mathbf{m}_{true}$ can be

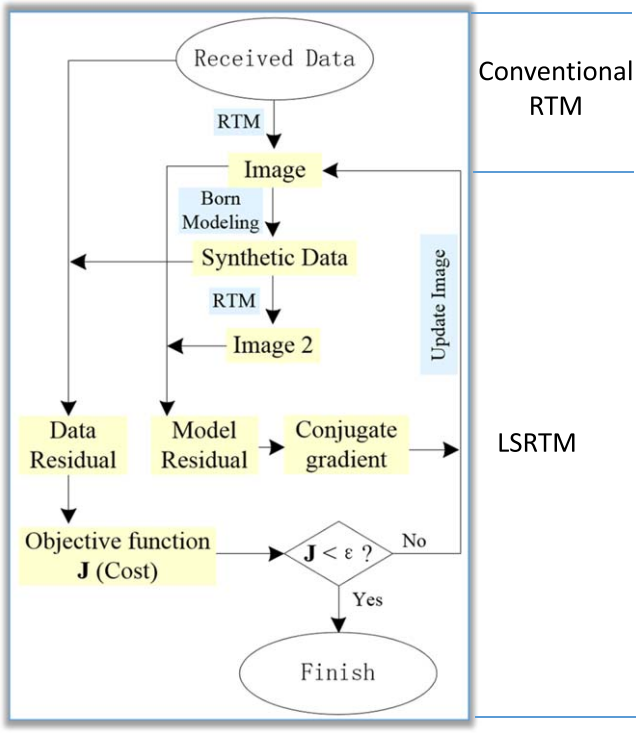


Figure 1. Schematic diagram of LSRTM.

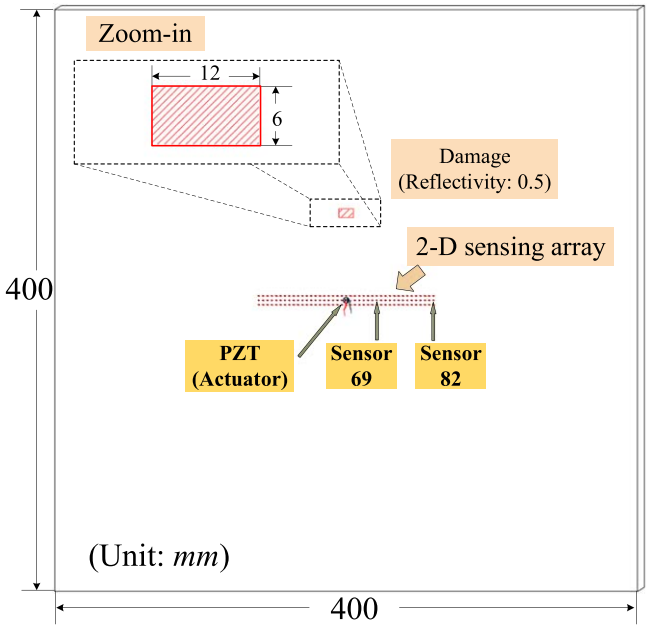


Figure 2. Illustration of the plate and the sensor array. (Sensors 69 and 82 will be referred to in a later section.)

estimated using the following equation

$$\mathbf{m}_{true} = (\mathbf{F}^T\mathbf{F})^{-1}\mathbf{m}_{mig} = (\mathbf{F}^T\mathbf{F})^{-1}\mathbf{F}^T\mathbf{d}_{obs}, \tag{4}$$

However, in practical applications, the inverse of $\mathbf{F}^T\mathbf{F}$ is usually too expensive to compute [49]. Instead of directly calculating equation (4) to find the solution $\mathbf{m}_{true}$ to equation (1), the solution can be alternatively and efficiently calculated through minimizing the following objective function

$$\mathcal{J}(\mathbf{m}) = \sum_e \frac{1}{2}\|\mathbf{d}_{obs} - \mathbf{F}\mathbf{m}\|^2, \tag{5}$$

which evaluates the misfit between observed data $\mathbf{d}_{obs}$ and the predicted data $\mathbf{F}\mathbf{m}$ using l_2 norm for the total number of actuators e. In this research, a single actuator was used such that $e = 1$. Then the Hessian matrix (second-order partial derivatives) of $\mathcal{J}$ is denoted as

$$\mathbf{H} = \mathbf{F}^T\mathbf{F}, \tag{6}$$

which will be used to simplify expressions in the next section.

2.1. CG method for LSRTM

To solve the least-squares problem in equation (5), a gradient optimization method such as steepest descent (SD) or CG [54, 55] is commonly used. The CG method converges faster compared with SD. The CG method updates the predicted reflectivity model in the following way:

$$\mathbf{m}_{k+1} = \mathbf{m}_k + \alpha_k\mathbf{p}_k, \tag{7}$$

where $\mathbf{m}_{k+1}$ and $\mathbf{m}_k$ are the $(k+1)$th and kth predicted reflectivity models, α_k is the step length for model updates, and $\mathbf{p}_k$ is the moving direction of the optimization process in the kth iteration. The model residual at the kth step is

$$\mathbf{r}_k = \mathbf{m}_{mig} - \mathbf{H}\mathbf{m}_k. \tag{8}$$

Note that $\mathbf{r}_k$ is also the negative gradient of $\mathcal{J}$ at $\mathbf{m}_k$. With a resemblance to Gram–Schmidt orthonormalization, in CG, the updating direction $\mathbf{p}_k$ is formed to ensure $\mathbf{p}_k$ is conjugate to all the previous directions p_i, $i < k$ with respect to matrix $\mathbf{H}$ ($\mathbf{H}$-orthogonal), i.e.

$$\mathbf{p}_k = \mathbf{r}_k - \sum_{i<k}\frac{\mathbf{p}_i^T\mathbf{H}\mathbf{r}_k}{\mathbf{p}_i^T\mathbf{H}\mathbf{p}_i}. \tag{9}$$

The step length α_k in equation (7) for model updating is calculated as

$$\alpha_k = \frac{\mathbf{r}_k^T\mathbf{r}_k}{\mathbf{p}_k^T\mathbf{H}\mathbf{p}_k}. \tag{10}$$

Then the model residual for the $(k+1)$th iteration can be updated using equations (8) and (7) as

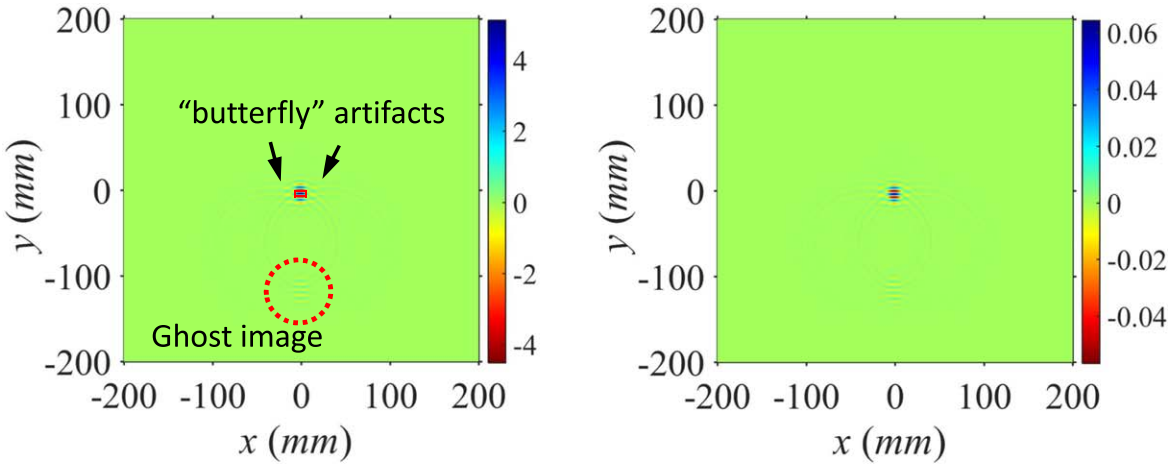
$$\mathbf{r}_{k+1} = \mathbf{r}_k - \alpha_k\mathbf{H}\mathbf{p}_k. \tag{11}$$

Similarly, the data residual can be updated as

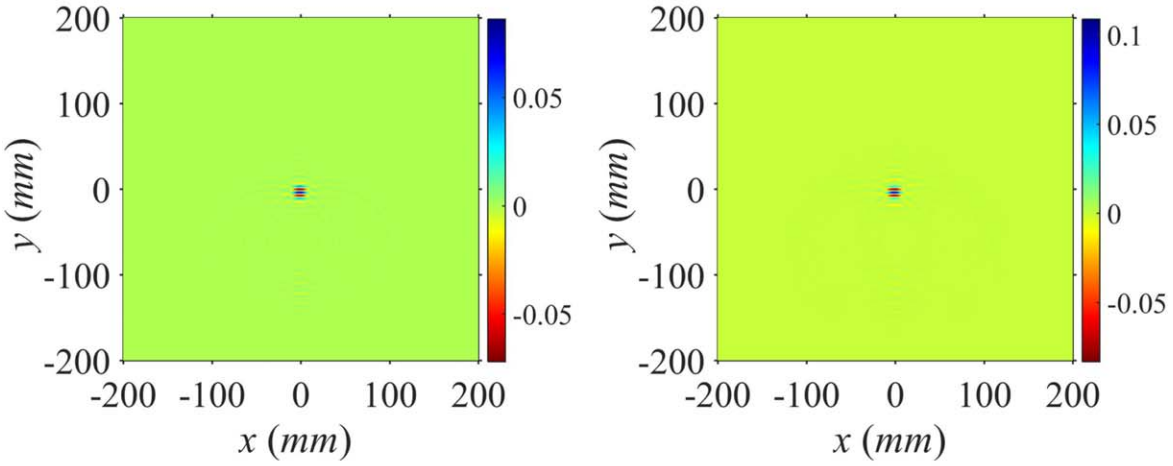
$$\mathbf{R}_{k+1} = \mathbf{d}_{obs} - \mathbf{F}\mathbf{m}_{k+1} = \mathbf{R}_k - \alpha_k\mathbf{F}\mathbf{p}_k. \tag{12}$$

Instead of calculating all previous moving directions using e.g. (9) for each iteration, it is possible to use a step length β_k to update the moving direction $\mathbf{p}_{k+1}$, i.e.

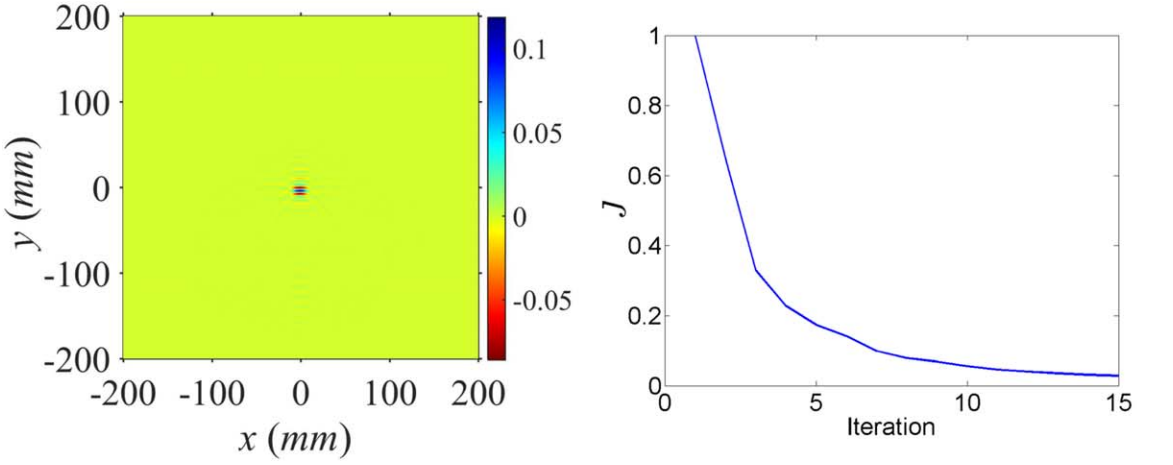
$$\mathbf{p}_{k+1} = \mathbf{r}_{k+1} + \beta_k\mathbf{p}_k, \tag{13}$$



(a) Conventional RTM (b) LSRTM 1st iteration

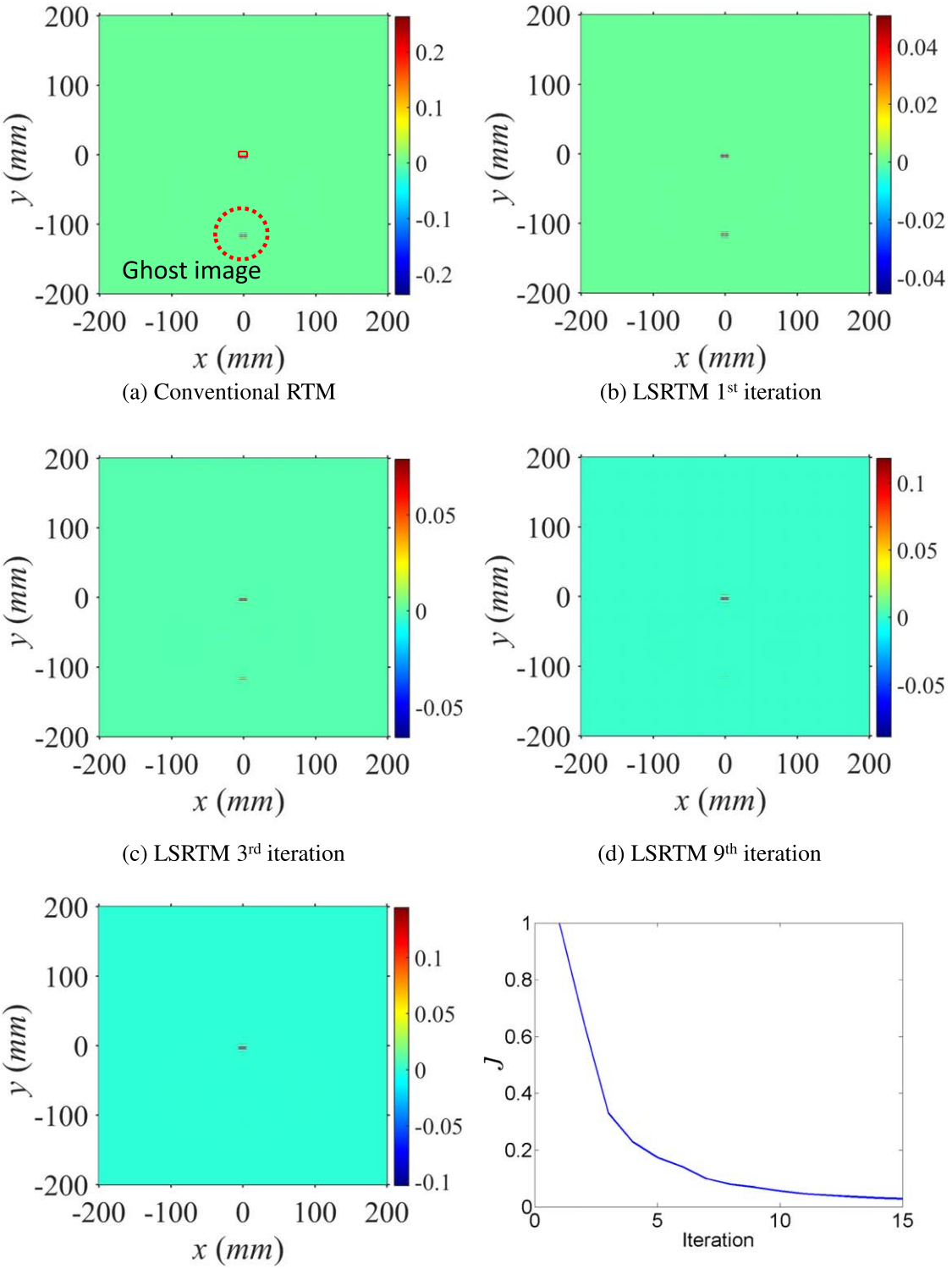


(c) LSRTM 3rd iteration (d) LSRTM 9th iteration



(e) LSRTM 15th iteration (f) Objective function J

Figure 3. Simulation results using an excitation signal with a center frequency of 100 kHz. (a) Conventional RTM image (the damage site is outlined by the red box in this subfigure), (b)–(e) LSRTM images from the 1st, 3rd, 9th and 15th iterations, and (f) the objective function from LSRTM for the first 15 iterations.



(a) Conventional RTM (b) LSRTM 1st iteration

(c) LSRTM 3rd iteration (d) LSRTM 9th iteration

(e) LSRTM 15th iteration (f) Objective function J

Figure 4. Simulation results using an excitation signal with a center frequency of 400 kHz. (a) Conventional RTM image (The damage site is outlined by the red box), (b)–(e) LSRTM images from the 1st, 3rd, 9th, and 15th iterations, and (f) the objective function from LSRTM for the first 15 iterations.

where β_k is calculated as

$$\beta_k = \frac{\mathbf{r}_{k+1}^T \mathbf{r}_{k+1}}{\mathbf{r}_k^T \mathbf{r}_k}. \qquad (14)$$

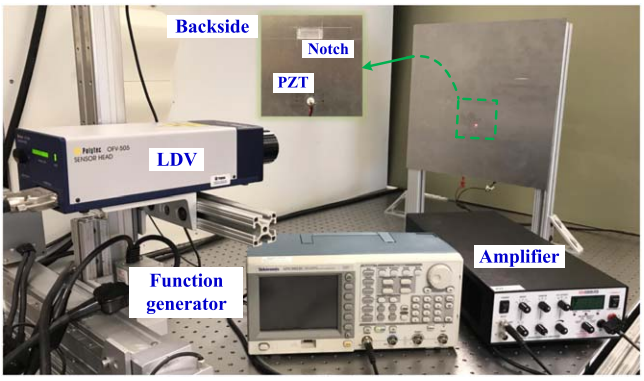


Figure 5. Experimental system for LSRTM imaging.

The schematic diagram of the LSRTM is shown in figure 1, where the top part is the same as the conventional RTM. The details of implementation for calculating the data residual, model residual, and predicted reflectivity model described in figure 1 are summarized in equations (11), (12), and (7), respectively.

3. Numerical simulation for damage imaging using LSRTM

In this section, the RTM and LSRTM damage imaging results using ultrasonic guided waves are compared. A finite difference algorithm was employed to simulate the flexural wave propagation based on Mindlin plate theory. Only A_0 mode Lamb waves exist in the simulation. Details about the finite difference algorithm can be found in [56]. The plate was modeled as aluminum 6061-T6 and the plate dimensions were 400 mm $\times$ 400 mm with a thickness of 2.2 mm (figure 2). The material properties were assigned to every grid in the finite difference algorithm.

All the material properties and geometrical information were known *a priori*. The actuator was simulated as grid points in the finite difference algorithm, corresponding to the area of the piezoelectric wafer in experiments. The finite difference algorithm inputs the excitation as time-dependent pressure distributed over the nodes to generate and record the forward wavefield. A 2.5-cycle Hanning-windowed toneburst excitation signal was applied to the actuator as an out-of-plane force. In the finite difference algorithm, the plate domain was discretized by a 400 $\times$ 400 mesh, with a 1 mm $\times$ 1 mm grid size. The actuator and the 2D scan points were modeled as grid points at their corresponding locations.

A 2D sensor array with 41 $\times$ 3 elements with a spacing of 3 mm was simulated to record the out-of-plane velocity. This 2D array design is sensitive to the incoming direction of the damage-scattered waves and reduces the ghost image on the opposite side of the array [15, 17]. This setup resembles the 2D array in the following experimental section, where the reception array was formed using the scanning points from a LDV.

A damage site was modeled as a constant reflectivity/scattering value based on the Born approximation [26, 57]. Thus, the scattered wavefield is propagated using source-time functions whose locations are within the damaged region, and values are calculated as the product between the incident wavefield and the corresponding scattering amplitude. In this section, the rectangular damage was 10 mm in length and 6 mm in width. The reflectivity value of the damage site was set to 0.5 and the center of the damage was 60 mm away from the actuator.

The results using an excitation signal with a center frequency of 100 kHz, using both RTM and LSRTM, are shown in figure 3. The reason to use 100 kHz is that the signal-to-noise ratio at this frequency is high using the piezoelectric wafers introduced in the experimental section. The conventional RTM image (figure 3(a)) illuminates the damaged area well. However, it also displays artifacts around the damaged region. On the opposite side of the array, a ghost image of the damage site can be spotted as well. Those artifacts and the ghost image are due to the limited aperture of the arrays. Limited-aperture arrays might be more practical than a full-aperture array, in cases where the inspection area is enclosed within the area surrounded by an array. However, a disadvantage of using a limited-aperture array is the generation of imaging artifacts due to the sidelobe of the array, which usually represents unwanted energy radiation in undesired directions [17].

Figures 3(b)–(e) shows the LSRTM results at four iterations. The image from the first iteration of LSRTM is similar to the conventional RTM results except for the amplitude. However, the artifacts around the damaged regions are reduced gradually over iterations. The imaging resolution has been improved because the illuminated region is closer to the original rectangular damage. The length of the 'butterfly' artifacts next to the damage site became shorter, and the intensity of the ghost image on the opposite side of the array becomes weaker, as shown in figures 3(c)–(e). For the 15th iteration, the ghost image effect is almost completely eliminated.

In figure 3(f), the normalized objective function, $\mathcal{J}$, calculated by equation (5), is monotonically decreasing. Since the Born approximation was used such that the formulated modeling was linear, the objective function $\mathcal{J}$ was expected to be convex. This is why the objective function approaches the global minimum in a monotonically decreasing manner. For NDE or SHM, this minimum leads to corresponding solutions (images) that are least-squares estimations of the damage model. Compared with another inversion-based imaging algorithm—full waveform inversion (FWI), whose optimization is a nonlinear problem [20, 58, 59]—LSRTM will converge to the global minimum as a linear optimization problem.

For the 100 kHz case, since the wavelength of the incident waves is relatively large, the imaged damage region was over-estimated by conventional RTM with those 'butterfly' artifacts (figure 3(a)). In contrast, LSRTM systematically reduced the over-estimation of the damage. To examine the influence of wavelength and the scattering effects at a different center frequency, another numerical simulation case was performed for the same damage site using an input signal

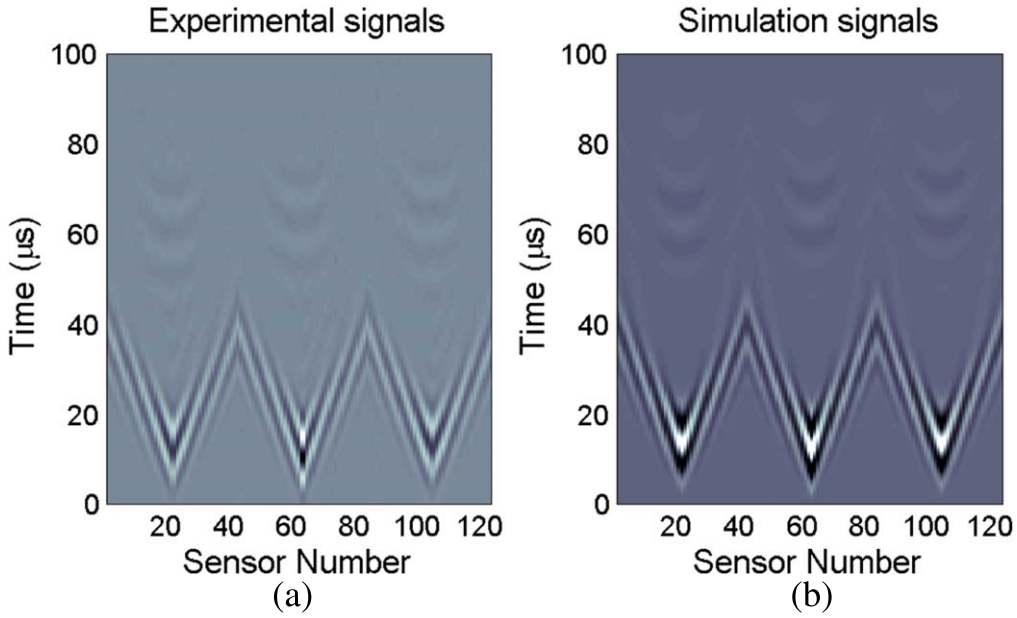


Figure 6. Signal comparisons from (a) experimental measurements and (b) simulation recording at 100 kHz.

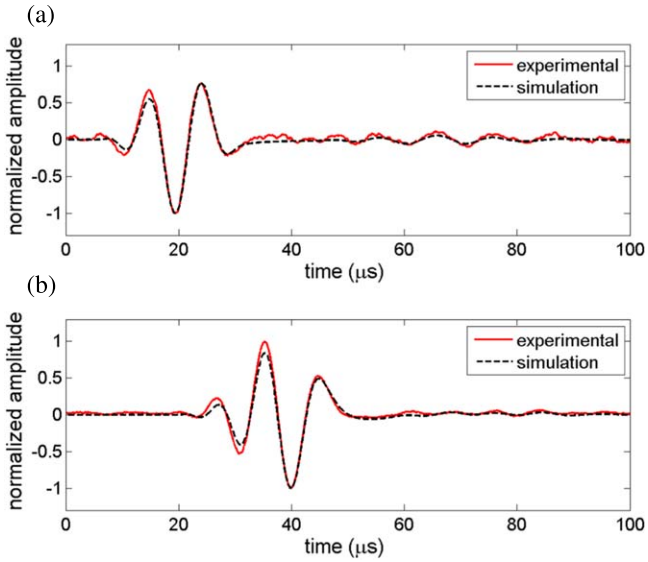


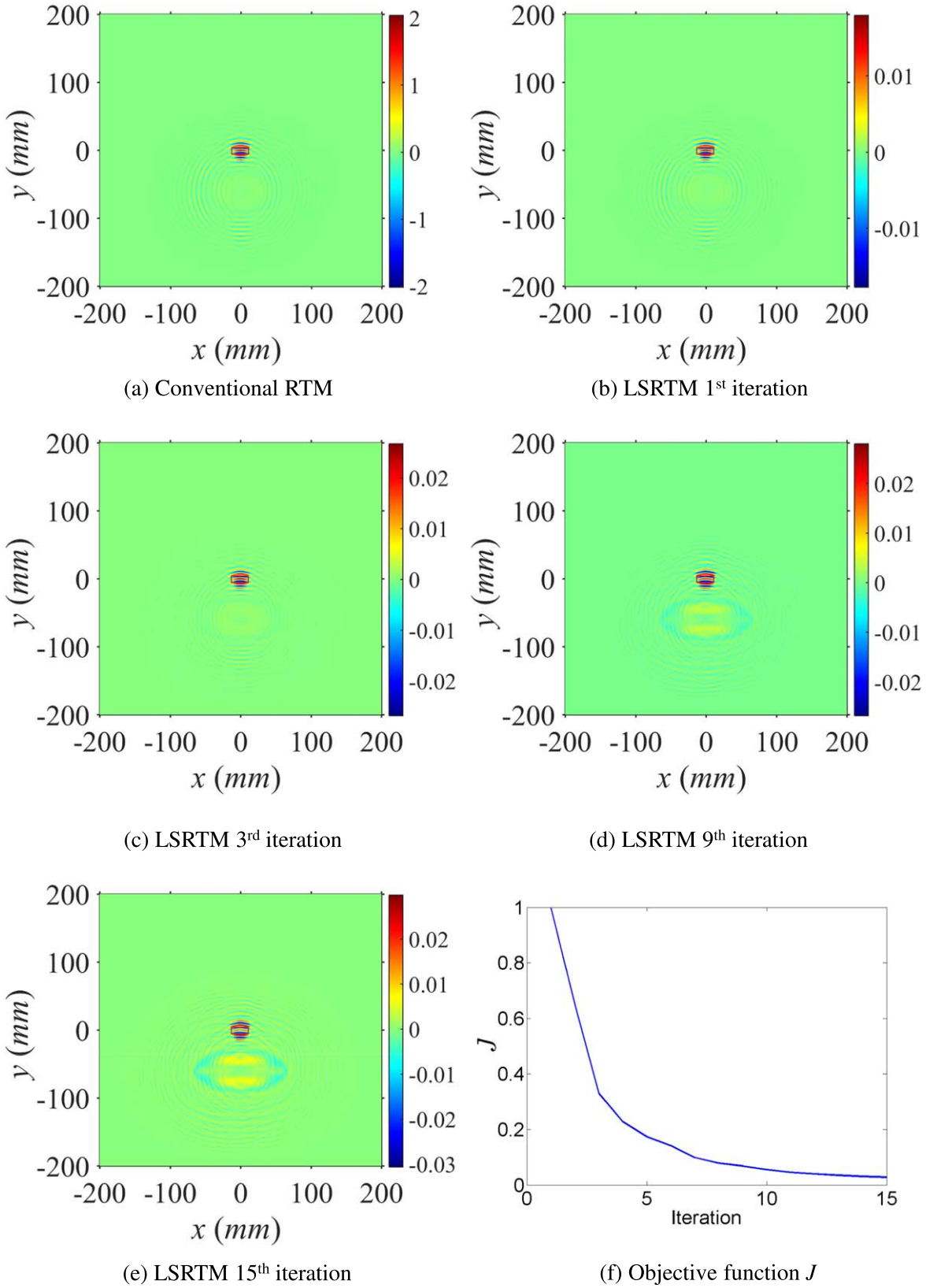
Figure 7. Comparison of the individual signals from the experiment and the simulation at (a) Sensor 69 and (b) Sensor 82 (see figure 2 for sensor positioning), with distances to the actuator center of 18 mm and 60 mm, respectively.

with a center frequency of 400 kHz. The conventional RTM results are shown in figure 4(a). The artifacts around the damage region became weaker and the image of the damage site was also more focused when compared to the 100 kHz case. However, the 'ghost' image on the opposite side of the array became stronger. Similar to the previous example, the first iteration of LSRTM (figure 4(b)) was similar to the conventional RTM image. As the number of iterations increased, the ghost images were suppressed further, until almost fully eliminated, as shown in figures 4(c)–(e). Although the artifacts around the damage regions of conventional RTM are already reduced at this higher frequency, they were still present. LSRTM compresses those artifacts further and the final image of LSRTM shows a well-focused damage region without any obvious artifacts or ghost images. In figure 4(f), the normalized objective function $\mathcal{J}$ is also monotonically decreasing for the 400 kHz case.

4. Experimental validation of the LSRTM technique

The aluminum alloy 6013-T6 test specimen is shown in figure 5. The plate had dimensions of 400 mm × 400 mm × 2.29 mm. A half-thickness notch with dimensions of 23 mm × 10 mm was placed in the plate as shown using electrical discharge machining. The data acquisition system included a 2D translational stage (IAI ROBO), a function generator (Tek AFG3000), a power amplifier (Krohn-Hite 7602), and an LDV (Polytec OFV-505). In order to receive the out-of-plane velocity on the surface of the plate, the LDV was oriented perpendicular to the plate. One piezoelectric wafer (Steiner Martins, Inc.) was attached to the center of the plate as the actuator, which was with dimensions of 7 mm in diameter and 0.3 mm in thickness.

To validate the wave propagation simulator implemented in this research, the experimentally acquired signals were compared with the simulated signals. The signals received by all the 123 sensors from both the experiment and the simulations are compared side-by-side in figure 6. The total acquisition time is 100 μs. The numbering of the sensors starts from the top left, then moves horizontally for each row, ending with the bottom right element, the same as the LDV scanning sequence. In this manner, the top row ranges from 1 to 41; the second row ranges from 42 to 82; the bottom row ranges from 83 to 123. Since there are three separate linear arrays horizontally aligned in the 2D array, both figures 6(a) and (b) show three interconnected regions. Signals between 0 and 40 μs mainly contain direct arrivals. After 45 μs, the sensors closer to the actuator began to receive the damage-



(a) Conventional RTM

(b) LSRTM 1st iteration

(c) LSRTM 3rd iteration

(d) LSRTM 9th iteration

(e) LSRTM 15th iteration

(f) Objective function J

Figure 8. Experimental results using an excitation signal with a center frequency of 100 kHz. (a) Conventional RTM image, (b)–(e) LSRTM images from the 1st, 3rd, 9th and 15th iterations, and (f) the objective function from LSRTM for the first 15 iterations. (The damage site is outlined by the red box.)

scattered signals, which had smaller amplitudes. Both the direct-arrivals and the damage-scattered signals were similar in the experimental and simulations cases.

For further illustration, signals at Sensors 69 and 82 with distances of 18 mm and 60 mm with respect to the center of the actuator, respectively, are shown in figure 7. Both the experimental and simulation signals were normalized by their maximum absolute value for easier comparison. The main peaks (direct arrivals) match well with each other. The experimentally measured signals had more noise, while simulation results were smoother. The numerical simulations were validated by the experimental results.

To perform back-propagation in RTM, the damage-scattered signals need to be time reversed. No baseline signals were available for this study since the notch was already cut before the experiment. Fortunately, the damage-scattered signals were not heavily superimposed with the direct arrivals. Simple mask filtering in time was applied to eliminate direct arrivals. For instance, the signal in-between 0 and 56, μs from Sensor 1 and the signal between 0 and 40, μs from Sensor 21 (the center element in the upper linear array) were set to zero. The backward wavefield was calculated using the finite difference algorithm with these time-reversed, damage-scattered signals as input at the sensor locations.

The resultant damage images using conventional RTM and LSRTM are shown in figure 8. As can be seen from figures 8(a), (b), the conventional RTM provides similar results as the first iteration of LSRTM. The damage location is correctly identified. Because the wavelength is relatively large, the main illuminated area was larger than that of the notch region. The ghost image on the other side of the array is also easily seen. Some 'ring' artifacts appear as well, which might be due to the incompletely extracted direct arrivals in the backpropagated signals. In figures 8(c)–(e), the ring artifacts are gradually balanced out using LSRTM. The ghost image is also eliminated. The illuminated damaged region became more focused, and the imaging resolution has been increased. These improvements potentially lead to easier automated detection and quantification of damage. Starting from figure 8(d), some large values begin to accumulate close to the array region, which should not be a critical problem, since guided waves are aiming for long-distance inspection or monitoring. The objective function $\mathcal{J}$ converges even faster in a monotonically decreasing manner than the simulations.

5. Conclusions and future work

LSRTM minimizes an objective function which quantifies the difference between the experimentally measured data and the data predicted by the model. The objective function in LSRTM monotonically decreased as the damage reflectivity was iteratively updated using the CG method. When compared with conventional RTM, the proposed LSRTM improved resolution and reduced artifacts using the same 2D sensor array. The ghost image due to the sidelobes of the 2D transducer array was significantly suppressed. Future work includes extending this LSRTM technique to composite materials.

Acknowledgments

The authors acknowledge the support provided by NASA's Convergent Aeronautics Solutions: Digital Twin project (#NNL09AA00A).

ORCID iDs

Jiaze He https://orcid.org/0000-0001-6198-0688

References

[1] Hu Z, Lu W, Thouless M D and Barber J R 2016 Effect of plastic deformation on the evolution of wear and local stress fields in fretting *Int. J. Solids Struct.* **82** 1–8
[2] Yeratapally S R, Glavicic M G, Argyrakis C and Sangid M D 2017 Bayesian uncertainty quantification and propagation for validation of a microstructure sensitive model for prediction of fatigue crack initiation *Reliab. Eng. Syst. Saf.* **164** 110–23
[3] Cawley P 2018 Structural health monitoring: closing the gap between research and industrial deployment *Struct. Health Monit.* **17** 1225–1244
[4] Khodaei Z S and Aliabadi M H 2016 A multi-level decision fusion strategy for condition based maintenance of composite structures *Materials* **9** 790
[5] Mitra M and Gopalakrishnan S 2016 Guided wave based structural health monitoring: a review *Smart Mater. Struct.* **25** 053001
[6] Yuan F-G 2016 *Structural Health Monitoring (SHM) in Aerospace Structures* (Duxford: Woodhead Publishing)
[7] Bhuiyan M Y and Giurgiutiu V 2017 Multiphysics simulation of low-amplitude acoustic wave detection by piezoelectric wafer active sensors validated by *in-situ* AE-fatigue experiment *Materials* **10** 962
[8] Liu Z, Dong T, Peng Q, He C, Li Q and Wu B 2018 AE source localization in a steel plate with the dispersive A0 mode based on the cross-correlation technique and time reversal principle *Mater. Eval.* **76** 371–82
[9] Zhou W, Li H and Yuan F-G 2016 An anisotropic ultrasonic transducer for Lamb wave applications *Smart Struct. Syst.* **17** 1055–65
[10] Zhou W, Yuan F-G and Shi T 2016 Guided torsional wave generation of a linear in-plane shear piezoelectric array in metallic pipes *Ultrasonics* **65** 69–77
[11] Ren B and Lissenden C J 2016 PVDF multielement Lamb wave sensor for structural health monitoring *IEEE Trans. Ultrason. Ferroelectr. Freq. Control* **63** 178–85
[12] Harb M S and Yuan F G 2017 Barely visible impact damage imaging using non-contact air-coupled transducer/laser Doppler vibrometer system *Struct. Health Monit.* **16** 663–73
[13] Liu Z, Yu H, Fan J, Hu Y, He C and Wu B 2015 Baseline-free delamination inspection in composite plates by synthesizing non-contact air-coupled Lamb wave scan method and virtual time reversal algorithm *Smart Mater. Struct.* **24** 045014
[14] Park B, Sohn H, Malinowski P and Ostachowicz W 2017 Delamination localization in wind turbine blades based on adaptive time-of-flight analysis of noncontact laser ultrasonic signals *Nondestruct. Test. Eval.* **32** 1–20

[15] He J and Yuan F-G 2016 A quantitative damage imaging technique based on enhanced CCRTM for composite plates using 2D scan *Smart Mater. Struct.* **25** 105022

[16] Williams W B, Michaels T E and Michaels J E 2017 Estimation and application of 2-D scattering matrices for sparse array imaging of simulated damage in composite panels *AIP Conf. Proc.* **1806** 020014

[17] He J and Yuan F-G 2016 Lamb-wave-based two-dimensional areal scan damage imaging using reverse-time migration with a normalized zero-lag cross-correlation imaging condition *Struct. Health Monit.* **16** (4) 444–457

[18] Rose J, Borigo C, Owens S and Reese A 2017 Rapid large area inspection from a single sensor position: a guided shear wave phased array scan *Mater. Eval.* **75** 671–8

[19] Brath A J, Simonetti F, Nagy P B and Instanes G 2017 Experimental validation of a fast forward model for guided wave tomography of pipe elbows *IEEE Trans. Ultrason. Ferroelectr. Freq. Control* **64** 859–71

[20] Ratassepp M, Rao J and Fan Z 2018 Quantitative imaging of Young's modulus in plates using guided wave tomography *NDT&E Int.* **94** 22–30

[21] Su Z, Ye L and Lu Y 2006 Guided Lamb waves for identification of damage in composite structures: a review *J. Sound Vib.* **295** 753–80

[22] Sharif-Khodaei Z and Aliabadi M H 2014 Assessment of delay-and-sum algorithms for damage detection in aluminium and composite plates *Smart Mater. Struct.* **23** 075007

[23] Yan F, Royer R L Jr and Rose J L 2010 Ultrasonic guided wave imaging techniques in structural health monitoring *J. Intell. Mater. Syst. Struct.* **21** 377–84

[24] Hall J S and Michaels J E 2010 Minimum variance ultrasonic imaging applied to an *in situ* sparse guided wave array *IEEE Trans. Ultrason. Ferroelectr. Freq. Control* **57** 2311–23

[25] Moll J, Schulte R T, Hartmann B, Fritzen C P and Nelles O 2010 Multi-site damage localization in anisotropic plate-like structures using an active guided wave structural health monitoring system *Smart Mater. Struct.* **19** 045022

[26] Belanger P, Cawley P and Simonetti F 2010 Guided wave diffraction tomography within the Born approximation *IEEE Trans. Ultrason. Ferroelectr. Freq. Control* **57** 1405–18

[27] Francis Rose L R and Wang C H 2010 Mindlin plate theory for damage detection: imaging of flexural inhomogeneities. *J. Acoust. Soc. Am.* **127** 754–63

[28] Huthwaite P and Simonetti F 2013 High-resolution guided wave tomography *Wave Motion* **50** 979–93

[29] Francis Rose L R, Chan E and Wang C H 2015 A comparison and extensions of algorithms for quantitative imaging of laminar damage in plates: I. Point spread functions and near field imaging *Wave Motion* **58** 222–43

[30] Fink M 1992 Time reversal of ultrasonic fields: I. Basic principles *IEEE Trans. Ultrason. Ferroelectr. Freq. Control* **39** 555–66

[31] He J and Yuan F-G 2016 Lamb wave-based subwavelength damage imaging using the DORT-MUSIC technique in metallic plates *Struct. Health Monit.* **15** 65–80

[32] Huang L and Labyed Y 2018 Windowed time-reversal music technique for super-resolution ultrasound imaging *US Patent* 9,955,943

[33] Labyed Y and Huang L 2012 Ultrasound time-reversal music imaging of extended targets *Ultrasound Med. Biol.* **38** 2018–30

[34] He J and Yuan F-G 2013 Damage identification for composite structures using a cross-correlation reverse-time migration technique. *The 9th Int. Workshop on Structural Health Monitoring* (Stanford, CA: Stanford University) p 98040V–11

[35] Baysal E, Kosloff D D and Sherwood J W C 1983 Reverse time migration *Geophysics* **48** 1514–24

[36] Claerbout J F 1992 *Earth Soundings Analysis: Processing Versus Inversion* vol 6 (Cambridge, MA: Blackwell Scientific Publications)

[37] Mulder W A and Plessix R-E 2004 A comparison between one-way and two-way wave-equation migration *Geophysics* **69** 1491–504

[38] Chan E, Francis Rose L R and Wang C H 2015 An extended diffraction tomography method for quantifying structural damage using numerical green's functions *Ultrasonics* **59** 1–13

[39] He J, Leser P E, Leser W P and Yuan F-G 2018 IWSHM 2017: damage-scattered wave extraction in an integral stiffened isotropic plate: a baseline-subtraction-free approach *Struct. Health Monit.* **17** (6) 1365–1376

[40] He J, Leckey C A C, Leser P E and Leser W P 2018 Multi-mode reverse time migration damage imaging using ultrasonic guided waves *Ultrasonics* (https://doi.org/10.1016/j.ultras.2018.08.005)

[41] Chattopadhyay S and McMechan G A 2008 Imaging conditions for prestack reverse-time migration *Geophysics* **73** S81–9

[42] Yan J and Sava P 2008 Isotropic angle-domain elastic reverse-time migration *Geophysics* **73** S229–39

[43] Duan Y and Sava P 2015 Scalar imaging condition for elastic reverse time migration *Geophysics* **80** S127–36

[44] Rocha D, Sava P and Nicolay Tanushev N 2015 Acoustic wavefield imaging using the energy norm *SEG Technical Program Expanded Abstracts 2015* (Society of Exploration Geophysicists) pp 4085–90

[45] Rocha D, Tanushev N and Sava P 2016 Isotropic elastic wavefield imaging using the energy norm *Geophysics* **81** S207–19

[46] Rocha D, Tanushev N and Sava P 2017 Anisotropic elastic wavefield imaging using the energy norm *Geophysics* **82** (3) S225–S234

[47] Dai W and Schuster G T 2013 Plane-wave least-squares reverse-time migration *Geophysics* **78** S165–77

[48] Kuehl H and Sacchi M 2002 Robust AVP estimation using least-squares wave-equation migration *SEG Technical Program Expanded Abstracts 2002* (Society of Exploration Geophysicists) pp 281–4

[49] Dong S, Cai J, Guo M, Suh S, Zhang Z, Wang B and Li Z 2012 Least-squares reverse time migration: towards true amplitude imaging and improving the resolution *SEG Las Vegas 2012 Annual Meeting* (*SEG Technical Program Expanded Abstracts 2012* SEG Technical Program Expanded Abstracts 2012) pp 1–5

[50] Rocha D and Sava P 2018 Elastic least-squares reverse time migration using the energy norm *Geophysics* **83** S237–48

[51] Rocha D, Sava P and Guitton A 2018 3D acoustic least-squares reverse time migration using the energy norm *Geophysics* **83** S261–70

[52] Volker A, van Zon T, Enthoven D, Verburg W, Chimenti D E and Bond L J 2016 1D profiling using highly dispersive guided waves *AIP Conf. Proc.* **1650** 754–60

[53] Aoki N and Schuster G T 2009 Fast least-squares migration with a deblurring filter *Geophysics* **74** WCA83–WCA93

[54] Nemeth T, Wu C and Schuster G T 1999 Least-squares migration of incomplete reflection data *Geophysics* **64** 208–21

[55] Symes W W 2008 Approximate linearized inversion by optimal scaling of prestack depth migration *Geophysics* **73** R23–35

[56] He J and Yuan F-G 2015 Damage identification for composite structures using a cross-correlation reverse-time migration technique *Struct. Health Monit.* **14** 558–70

[57] Gubernatis J E, Domany E, Krumhansl J A and Huberman M 1977 The Born approximation in the theory of the scattering of elastic waves by flaws *J. Appl. Phys.* **48** 2812–9

[58] Rao J, Ratassepp M and Fan Z 2016 Guided wave tomography based on full waveform inversion *IEEE Trans. Ultrason. Ferroelectr. Freq. Control* **63** 737–45

[59] Tromp J, Komattisch D and Liu Q 2008 Spectral-element and adjoint methods in seismology *Commun. Comput. Phys.* **3** 1–32